



# Estimation of Fracture Permeability from Aperture Distributions for Rough and Partially Cemented Fractures

Christopher J. Landry<sup>1</sup> · Maša Prodanović<sup>1,3</sup> · Zuleima Karpyn<sup>4</sup> · Peter Eichhubl<sup>2</sup>

Received: 28 March 2022 / Accepted: 6 January 2024 / Published online: 25 February 2024  
© The Author(s), under exclusive licence to Springer Nature B.V. 2024

## Abstract

Natural fractures in subsurface reservoirs are frequently partially cemented with mineral precipitates, and it is unclear if fracture permeability models developed for rough barren fractures are applicable for fractures where roughness originates from cement linings. Here, we use a digital rock physics workflow to quantify the error in fracture permeability predicted by these models for five digitally synthesized rough fractures and four fractures imaged using three-dimensional X-ray computed microtomography. Samples include a rough, artificially-induced barren fracture in sandstone, a cement-lined natural fracture in limestone sampled from outcrop, and two cement-bridged natural fractures in tight-gas sandstones sampled from reservoir core. The images are then processed, segmented, characterized to determine statistical moments of the aperture distribution, and used in lattice Boltzmann model flow simulations. We address complications in measuring aperture distributions from images when the fracture pore space morphology deviates from the typical theoretical description of rough fractures and evaluate three different methods of measuring local aperture. The alternative cubic law using the nominal mean aperture is found to overestimate fracture permeability by upwards of one to two orders of magnitude, while the fracture permeability models using statistical moments of the aperture distribution are far more accurate for both rough barren and partially cemented fractures. We also define an empirical description of the upper and lower bounds of fracture permeability estimates as a function of relative roughness that is applicable to both rough barren and partially cemented fractures.

**Keywords** Mineralized fracture · Single-phase flow · Cubic law · Lattice Boltzmann model · Digital rock physics

---

✉ Christopher J. Landry  
christopher.landry@utexas.edu

<sup>1</sup> Center for Subsurface Engineering and the Environment, The University of Texas at Austin, Austin, TX 78712, USA

<sup>2</sup> Bureau of Economic Geology, Jackson School of Geosciences, The University of Texas at Austin, Austin, TX 78757, USA

<sup>3</sup> The Hildebrandt Department of Petroleum and Geosystems Engineering, The University of Texas at Austin, Austin, TX 78712, USA

<sup>4</sup> John and Willie Leone Family Department of Energy and Mineral Engineering, The Pennsylvania State University, University Park, PA 16802, USA

## 1 Introduction

Fractures exist in rock at scales that range from the micrometers to kilometers. Numerical methods are commonly used to investigate the influence of fractures on mass transport and fluid flow in porous rock at multiple scales. Using numerical simulation methods, the relationship between the spatial distribution of fractures and their effect on fluid flow and mass transport can be explored by explicitly representing fractures in a simulation volume. The spatial distribution of fractures in these numerical simulations are typically informed via stochastic realizations (de Dreuzy et al. 2012; Ebigbo et al. 2016; Hyman et al. 2015; Lang et al. 2014; Lei et al. 2015; Olorode et al. 2020), direct translation from outcrop observations (e.g. Belayneh et al. 2009; Bisdorf et al. 2014; Geiger and Matthai 2014), or geomechanical simulation (Dahi Taleghani and Olson 2014; Fu et al. 2013; Kresse et al. 2013; Paluszny and Matthai 2010; Thomas et al. 2020). The flow properties of the fractures are informed using fracture permeability models that typically invoke some form of the so-called ‘cubic-law’ to relate the fracture aperture (or statistical moments of the fracture aperture distribution) to fracture permeability.

Fracture permeability models that are typically employed in fractured rock flow simulations were originally developed for rough barren fractures, however, fractures in the subsurface commonly accumulate mineral cements, both during and after fracture opening. The cementing of subsurface fractures can occur on geologic time-scales (Becker et al. 2010; Fall et al. 2012, 2014; Gale et al. 2014; Hood et al. 2003; Lander and Laubach 2015; Lorenz 2003; Luczaj et al. 2006; Wennberg et al. 2016) and over much smaller time scales as a result of CO<sub>2</sub> geo-sequestration (e.g. Cao et al. 2015; Jones and Detwiler 2016; Matter and Kelemen 2009; Phillips et al. 2013) and geothermal engineering projects (e.g. Borgia et al. 2012; Pandey et al. 2015; Taron and Elsworth 2009). Unlike rough barren fractures, the changes to the morphology and topology of the fracture pore space of partially cemented fractures is driven by chemical precipitation instead of mechanical processes. With increasing cementation, fracture porosity becomes partially occluded by the formation of cement linings and cement bridges that can span the fracture from wall to wall leading to a partially connected porous network within the fracture (Gale et al. 2014; Lander and Laubach 2015; Laubach et al. 2004). Bench-scale flow experiments have demonstrated that changes to the fracture pore space morphology and topology as a result of cementation can significantly influence the flow properties of fractures (Cao et al. 2015; Jones and Detwiler 2016; Luquot et al. 2013; Noiriél et al. 2010; Tokan-Lawal et al. 2015a; Tokan-Lawal et al. 2016a, 2016b; Yoon et al. 2012). These experiments have demonstrated, but not quantified, the relationship between fracture pore space morphology/topology and permeability for partially cemented fractures.

The relationship between fracture size and aperture and permeability can substantially influence flow and transport in fracture networks (e.g. Cvetkovic and Frampton 2012; Hyman et al. 2016). Therefore, inaccuracy in fracture permeability estimates from the geometric description of the fracture size, aperture and volume can influence the results of numerical simulation of flow and mass transport in fractured rock. To properly account for these inaccuracies, and to establish their influence on numerical simulation results, it would be advantageous to quantify the error of fracture permeability models, and, if reasonable, establish upper and lower bounds on fracture permeability estimates. The establishment of upper and lower bounds on fracture permeability estimates from aperture distributions for rough fractures has been theoretically and numerically investigated by multiple authors with the general consensus that there is a non-linear increase in deviation between

the mechanical and hydraulic aperture (i.e. permeability) with increasing relative roughness (or conversely, decreasing 'relative smoothness') and contact fraction (Brown 1987; Méheust and Schmittbuhl 2001; Thompson and Brown 1991; Tsang 1984; Witherspoon et al. 1980; Zimmerman and Bodvarsson 1996; Zimmerman et al. 1992). As is elaborated on in the previously referenced studies, this error is associated with not considering the spatial arrangement of local apertures.

For large barren fractures with relatively smooth walls (i.e. the variation in local aperture due to wall roughness is an order of magnitude smaller than the overall aperture), the rate of flow in the fracture can be defined fairly confidently with only knowledge of the fracture wall separation (i.e. the nominal aperture). For increasingly rough fractures, the local aperture variation results in complex flow patterns, and the flow rate cannot be approximated by the nominal aperture alone. Zimmerman and Bodvarsson (1996) attempted to account for this complex flow using models that employed measurements of the local aperture distribution, specifically the mean and standard deviation of the aperture distribution in conjunction with a correction for 'contact area' or asperities. These models estimated the hydraulic aperture (i.e. fracture permeability) with significantly greater accuracy than smooth-plate models informed only by the aperture mean. Méheust and Schmittbuhl (2001) compared the hydraulic aperture with the geometrically measured mean mechanical aperture and found the deviation from the geometrically measured aperture and subsequent estimated flow rate in fractures could be well-described as a function of the relative roughness, thus providing a quantitative measure of the error in the a-priori estimate of fracture permeability from measurements of local of aperture. These studies, amongst many others, offer a framework for understanding the error expected from fracture permeability models based on measurements of fracture geometry; however, they are based on rough fractures hosted by relatively low-permeability rock (e.g. granite). It should be noted that the measurement of fracture permeability for fractures hosted by relatively high permeability rock can be difficult due to the flow in the matrix enhancing flow in the fracture, specifically when the fracture aperture approaches the pore size of the matrix rock (Landry and Karpyn 2012), which can lead to difficulty in decoupling fracture and matrix flow in benchtop measurements of fractured high permeability rock (e.g. sandstones).

It remains unclear if the fracture permeability models typically used to estimate fracture permeability from the aperture distribution of rough barren fractures are applicable to partially cemented fractures. Although the morphology and topology of partially cemented fractures differs from rough barren fractures, they can both be viewed as two-dimensional conductive mediums, wherein local conductivity is a function of local aperture. This similarity, and the subsequent fracture permeability estimate, is dependent on the definition of the 'local aperture'. It is relatively simple to define the local aperture in a rough walled fracture, but it is not entirely clear how these apertures should be measured in the complex pore space of partially cemented fractures.

This investigation is a study of the relationship between fracture pore space geometry and permeability. The X-ray computed microtomography (XCMT) fracture images used here are limited in their field of view, and likely are smaller than the 'correlation length' (the definition of this length for partially cemented fractures is somewhat ambiguous), introducing a possible sampling error related to field of view that is common to high-resolution images of natural porous media. The fracture permeability models evaluated here use the first and second central moments of the aperture distribution to estimate permeability, they do not consider the spatial distribution of apertures, or the arrangement of the apertures. Therefore, we expect there to be error in the fracture permeability estimates, and our goal is to quantify this error. Our objectives are to (1) compare fracture permeability

model estimates for rough barren and partially cemented fractures to measurements determined by pore-scale flow simulation, and (2) use these results to establish upper and lower bounds on fracture permeability model estimates for rough barren and partially cemented fractures. In the following, we use a digital rock physics workflow to measure fracture permeability. Three-dimensional XCMT images of rough barren, cement-lined, and cement-bridged fractures, as well as digitally synthesized fractures that mimic physically measured fractures, are used to measure aperture distributions and determine permeability through image-based lattice Boltzmann model (LBM) flow simulations. The use of ‘real’ fractures is deliberate. We are interested in quantifying the extent of fracture permeability model error for real fractures rather than relating permeability to statistical correlations in theoretical rough fracture geometries.

## 2 Methods

### 2.1 Image processing

Four three-dimensional X-ray computed microtomography (XCMT) images of fractures and five digitally synthesized fractures were processed and analyzed for fracture permeability estimation and numerical flow simulation. The imaged fractures include an artificially-induced barren tensile fracture in Berea sandstone (Fig. 2a) (Karpyn et al. 2007; Karpyn 2016), a calcite-lined fracture in limestone of the Niobrara Formation collected in outcrop (Fig. 2c) (Tokan-Lawal et al. 2015a; Tokan-Lawal et al. 2016a, b), and two quartz-bridged fractures, one sampled from Travis Peak sandstone (Tokan-Lawal et al. 2015a, b), a tight-gas sandstone reservoir core (Fig. 2e), and the other sampled from Mesaverde Group tight-gas sandstone core (Fig. 2g). The first three images were obtained from the Digital Rocks Portal and further information regarding these fractures can be found in the above referenced studies. The fracture sample of Upper Cretaceous Mesaverde Group sandstone was collected from core at a depth of about 3.8 km in the Piceance basin, Colorado. More information on similar fractures in this formation can be found in Fall et al. (2014). The Mesaverde fracture XCMT image used in this study was obtained at the UTCT, High-Resolution X-Ray Facility, The University of Texas at Austin. The five digitally synthesized fractures were created using the open source software SynFrac, using the input parameters for fractures A, B, C, D, E from Ogilvie et al. (2006). SynFrac creates rough fracture surfaces based on the spectral synthesis method (Brown 1995), which correlate at longer wavelengths but vary at smaller wavelengths as observed in real fractures. The SynFrac parameters used here are summarized in Ogilvie et al. (2006) their Table 1. These synthesized fractures mimic artificially-induced barren mode 1 fractures in (A) red granite, (B) syenite, (C) gabbro, (D) medium-grained, durable sandstone, and (E) granodiorite.

Each XCMT image of a fracture (Fig. 1a, c, e, g) was first rotated and tilted to align the fracture plane with the image grid. For the rough barren fracture in Berea sandstone, the image was also resampled to produce a cubic image grid. Following alignment and resampling, salt-and-pepper-type noise was reduced using two-dimensional anisotropic diffusion—an edge-preserving smoothing algorithm. The well-separated solid (higher attenuation peak) and pore (lower attenuation peak) populations of the images (Fig. 1i) simplified segmentation, in other words, only a small portion of the images was not readily attributable to either the pore or solid populations. Therefore, segmentation was carried out using simple thresholding (Fig. 1b, d, f, h), with the threshold taken at the CT number (relative

**Table 1** XCMT image and SynFrac subsamples used in aperture measurements and numerical simulations

Fracture name (type)	Original segmented image size ( $\delta$ )	Voxel side length ( $\delta$ ) ( $\mu\text{m}$ )	Subsample number (subsample size, $L \times w$ [ $\delta$ ])	Close [-] or open [+] [ $\delta$ ]
Berea (Rough barren)	$800 \times 3085 \times 220$	27.43	4 ( $800 \times 800$ )	[0, +10, +20, +40, +60, +80, +100]
SynFrac (A-E) (Rough barren)	$1000 \times 1000 \times (75, 50, 78, 90, 52)$	97.7	1 ( $1000 \times 1000$ )	[0]
Niobrara (Cement-lined)	$440 \times 570 \times 220$	26.69	2 ( $440 \times 440$ )	[-40, -30, -20, -10, 0, +25, +50, +100]
Travis Peak (Cement-bridged)	$900 \times 1775 \times 305$	5.97	4 ( $900 \times 900$ )	[0]
Mesaverde (Cement-bridged)	$700 \times 879 \times 350$	3.16	2 ( $700 \times 700$ )	[0]

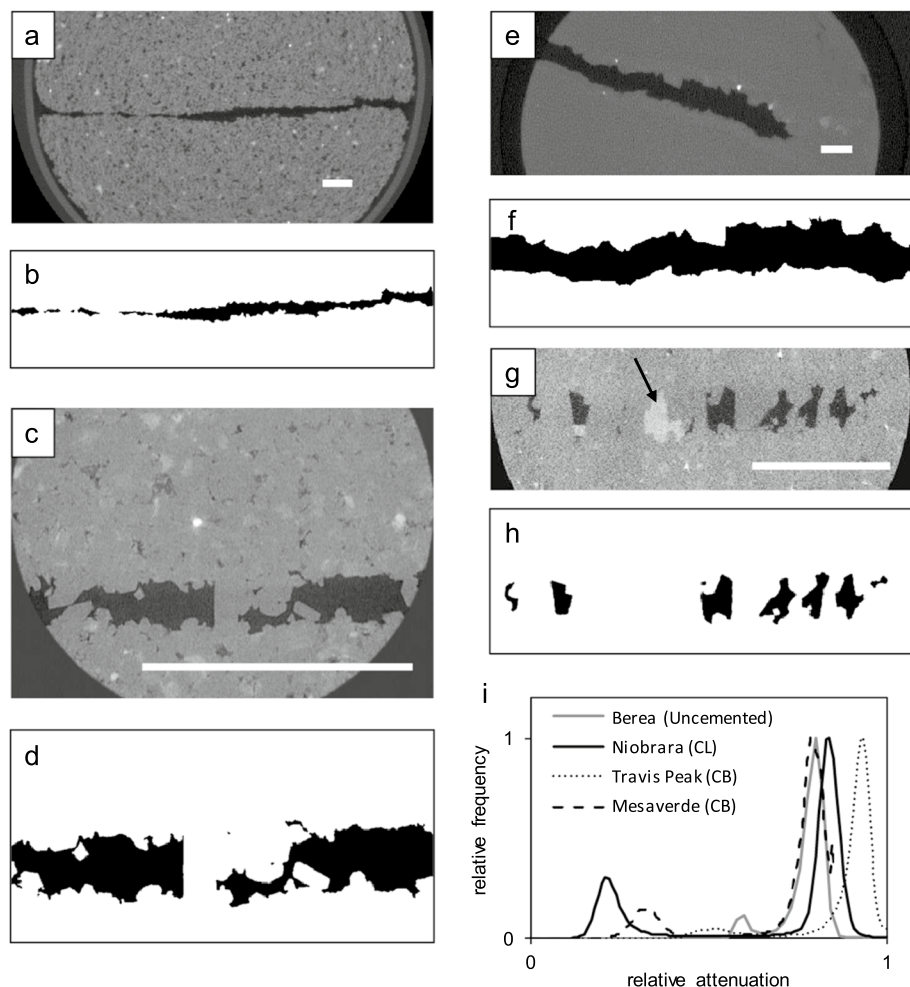


**Fig. 1** Example images and CT number distributions. Cross-sectional XCMT image and segmented image for: **a, b** rough artificial fracture in Berea sandstone, **c, d** cement-bridged fracture in Mesaverde tight sandstone, **e, f** cement-lined fracture in Niobrara limestone, and **g, h** cement-bridged fracture in Travis Peak sandstone. **i** Relative attenuation distributions for XCMT images. All scale bars indicate 2 mm. Note the Travis Peak fracture contains both quartz cement bridges and calcite cement (arrow) partially filling remaining fracture porosity

attenuation) correlating with the minimum between the two population peaks. The SynFrac fractures were output as  $512 \times 512$  fracture face location arrays and translated into discrete three-dimensional image grids using in-house MATLAB scripts. All the SynFrac fractures were downsampled during translation to image grids using linear interpolation between fracture face locations resulting in image grids of size  $1024 \times 1024 \times Z$ , where  $Z$  varies between SynFrac fractures, before being cropped. After translation to an image grid no further processing is required. Images of the SynFrac fractures are shown in Fig. 2a–e.

After segmentation, the rough barren and cement-lined fractures were further digitally manipulated to increase and decrease the nominal aperture, resulting in a decrease and



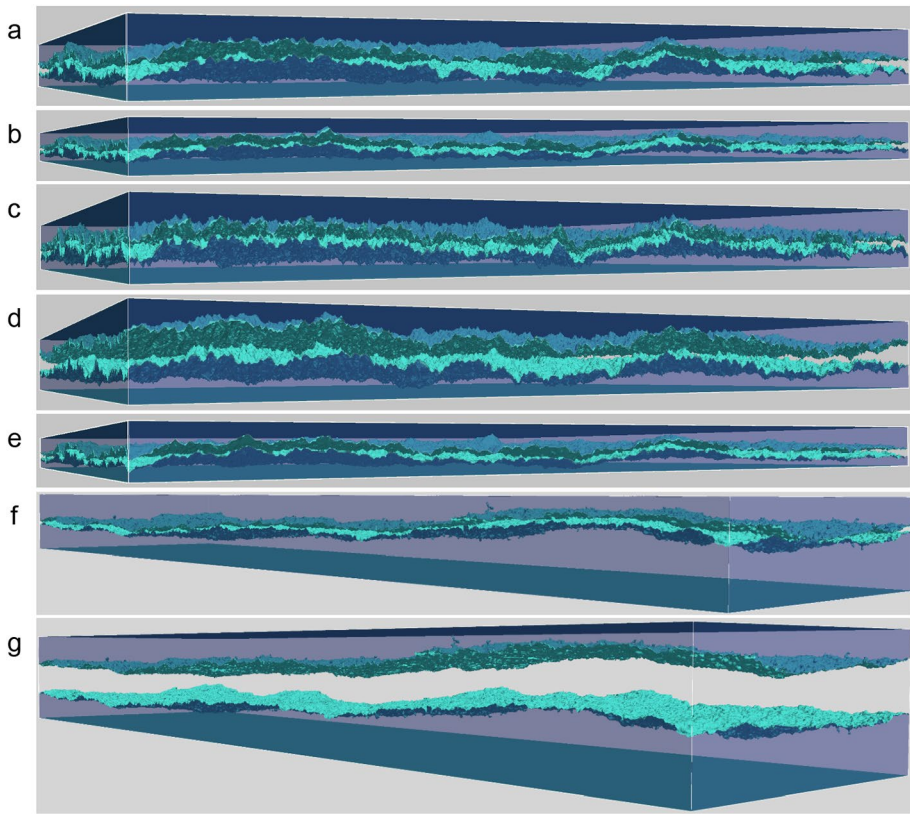


**Fig. 2** Three-dimensional image renderings of the rough barren fractures. **a–e** Three dimensional image renderings of the SynFrac A, B, C, D, E, **f** the rough barren fracture in Berea and **g** a digitally opened rough barren fracture in Berea image (open =  $100\delta$ )

increase in relative roughness, respectively. The rough barren fracture in Berea was digitally opened in the image grid direction orthogonal to the fracture plane in discrete steps of voxel resolution  $\delta$  to decrease the relative roughness, as shown in the images presented in Fig. 2f–g. This is equivalent to increasing the kinematic aperture, which is the distance of separation between the two fracture surfaces in an opening-mode fracture. The rough barren fracture is not digitally closed because the two-sides are in contact (full inelastic closure), and, unlike cement-lined fractures, the location of the solid/pore space interface is determined by this contact. The cement-lined fracture was both digitally opened and closed to decrease and increase the nominal aperture, respectively (Fig. 3). Under the assumption that the cement lining of opposing faces would overlap, this is the equivalent of either increasing/decreasing the kinematic aperture while maintaining a constant cement lining thickness or increasing/decreasing the lining thickness while maintaining the kinematic aperture. The cement-bridged fractures are not amenable to simple translation-based variation in kinematic aperture because the bridges constrain the kinematic aperture. These fractures are only used in this investigation as imaged (Fig. 4). The SynFrac fractures were not digitally dilated, as their relative roughness was already relatively low. For all imaged fractures the images are then subsampled, such that the subsamples have equal side lengths,

**Fig. 3** Three-dimensional image renderings of cement-lined fracture in Niobrara limestone. Showing the digitally closed image on top (closure =  $40\delta$ ), original image in the middle, and a digitally opened image on bottom (open =  $100\delta$ )

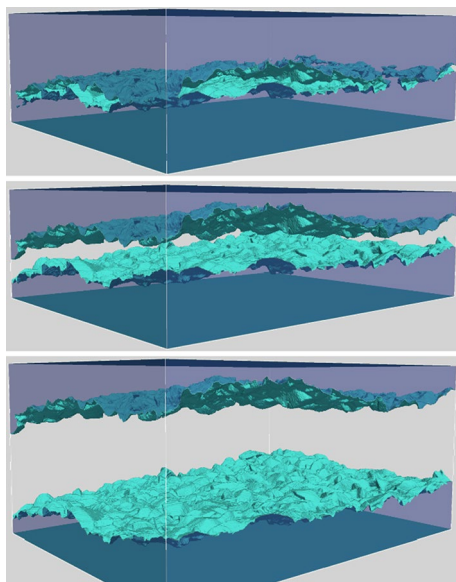
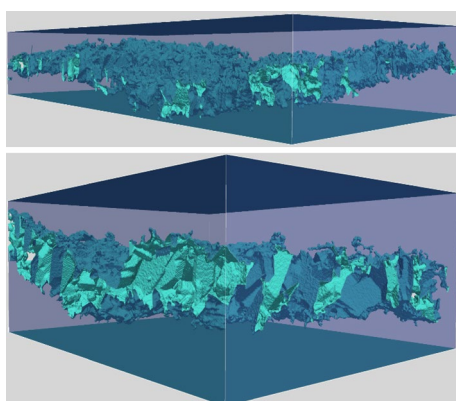


**Fig. 4** Three-dimensional image renderings of cement-bridged fractures. Showing Travis Peak sandstone (top), and Mesaverde sandstone (bottom)



$L = w$ , with minimum subsample overlap. This resulted in 28, 16, 4, and 2 total subsamples for the rough barren Berea, cement-lined Niobrara, and the cement-bridged Travis Peak and the Mesaverde tight sandstone fractures, respectively. Subsamples were then translated to flow simulation lattices and used to measure aperture distribution. A summary of subsample image sizes and voxel sizes ( $\delta$ ) for all fractures can be found in Table 1.

## 2.2 Fracture Permeability Models and Fracture Aperture Measurement

For numerical flow simulation where fractures are explicitly modeled, each fracture (or portion of) requires an assigned transmissivity. The transmissivity is a product of fracture permeability, which is a measure of hydraulic conductivity, and the cross-sectional area of flux. Here, we describe fracture permeability models in the context of



transmissivity, elaborated on below, because there is a subtle difference between the two when measuring the apertures of the fractures imaged here. Flow in rough fractures typically is described by making use of the cubic law, for which the volumetric flux,  $Q$ , between two parallel plates, assuming laminar incompressible flow is,

$$Q = \frac{wh^3 \Delta P}{12 \mu L}, \quad (1)$$

where  $h$  is the separation distance between the plates,  $\mu$  is the dynamic viscosity,  $w$  is the width of the parallel plates (orthogonal to flow), and  $\Delta P/L$  is the pressure gradient in the direction of flow. The cubic law is similar to Darcy's law, with a cross-sectional area of flux,  $A = wh$ , and a permeability,  $k = h^2/12$ , where the transmissivity can then be defined as the product of the permeability and cross-sectional area of flux,

$$T = kA = \frac{wh^3}{12}. \quad (2)$$

For a rough fracture it has been proposed that the fracture transmissivity can be estimated by substituting the separation distance of the parallel plate model with the mean aperture,  $\langle h \rangle$ ,

$$T = \frac{w\langle h \rangle^3}{12}. \quad (3)$$

where the mean aperture is equal to either the arithmetic, geometric, or harmonic mean of the aperture distribution (Brown 1987; Konzuk and Kueper 2004; Méheust and Schmittbuhl 2001; Thompson and Brown 1991; Witherspoon et al. 1980; Zimmerman et al. 1991; Zimmerman and Bodvarsson 1996). This formulation of the fracture transmissivity has been described as the 'alternate' cubic law (ACL) (Brown 1987). For the purposes of this study, we will evaluate the ACL estimates of fracture transmissivity under two scenarios, (1) assuming only the fracture volume,  $V$ , and spatial extent of the fracture (or portion of) are known, and (2) assuming the aperture distribution is known. Under scenario 1 the nominal mean aperture can be calculated as  $\langle h \rangle = h_n = V/wL$ . When the fracture aperture varies primarily orthogonal to the direction of flow, the fracture transmissivity tends towards the high-end estimate given by the arithmetic mean, and when varying primarily parallel to the direction of flow it will tend towards the harmonic mean. Previous researchers have found that the geometric mean,  $h_G$ , can be the more accurate predictor of fracture transmissivity (Konzuk and Kueper 2004; Piggott and Elsworth 1992; Zimmerman and Bodvarsson 1996).

The actual transmissivity can be defined by the hydraulic aperture,  $h_h$ ,

$$T = \frac{wh_h^3}{12}, \quad (4)$$

where the hydraulic aperture is the equivalent aperture for flow between parallel plates calculated from a measured effective hydraulic conductivity, it is not a geometric measurement. Treating the transmissivity of a fracture as similar to that of a two-dimensional permeable medium (Dagan 1979), Zimmerman and Bodvarsson (1996) derived an estimate of the hydraulic aperture assuming the cube of the local aperture is equal to the local transmissivity,

$$h_h^3 = h_A^3 \left( 1 - 1.5 \frac{\sigma^2}{h_A^2} \right). \quad (5)$$

where  $h_A$ , and  $\sigma$  are the arithmetic mean and standard deviation of the aperture distribution. The Zimmerman and Bodvarsson (1996) hydraulic aperture estimate is derived assuming a lognormal aperture distribution, but they argue that it remains a useful approximation regardless of the aperture distribution. The estimates of fracture transmissivity given by Eqs. (3)–(5) ignore any spatial correlations of the aperture field. Although a significant body of work has shown that rough fracture surfaces are fractal with aperture fields that contain long-range correlations (e.g. Brown 1995; Brown and Scholz 1985; Ogilvie et al. 2006), we did not attempt to use any models that include geometric information beyond the aperture distribution. We are interested in the accuracy of fracture permeability models when only the aperture distribution is known or assumed—as may be the case for fractures in subsurface reservoirs.

Measuring the aperture distribution of fractures from three-dimensional images is complicated by the morphological deviation of rough and partially cemented fractures from model descriptions of rough fracture pore spaces. Rough fractures are typically theorized as two rough surfaces wherein each point ( $i, j$ ) on a plane running parallel to the fracture corresponds with exactly one point on each fracture wall (Fig. 5a). For some rough, and particularly, for partially cemented fractures, this description is often violated (Fig. 5b). These deviations in morphology can complicate the definition of ‘aperture’—any particular position on a plane running parallel to the fracture may be associated with multiple aperture measurements (Fig. 5b). Also, when the aperture is measured as the distance between the walls normal to the plane running parallel to the fracture—sometimes referred to as the ‘vertical’ aperture—the estimated transmissivity may be overestimated. Alternatively, it has been proposed that the ‘perpendicular’ aperture,  $h_{\perp}$ , better approximates the local transmissivity (Fig. 5a, b) and therefore, as demonstrated in Konzuk and Kueper (2004), results in more accurate fracture transmissivity estimates.

For the images evaluated here,  $i, j, k$  are Cartesian coordinates of the three-dimensional image grid oriented with the  $x$ – $y$  plane parallel to the fracture. The fracture aperture measurements are taken at every image grid point  $i, j$ . By imposing this measurement strategy, wherein, perpendicular apertures are measured at equidistant points along a plane running parallel to the fracture (i.e.  $i, j$  in Fig. 5), we propose a ‘cross-sectional area correction’ should be applied to the definition of the fracture transmissivity. To demonstrate this correction, in

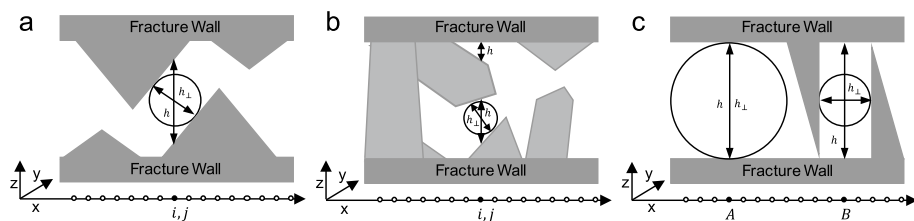


**Fig. 5** Cartoons illustrating aperture measurements. **a** Cartoon of a cross section of a rough fracture as typically theorized with each point along the image grid ( $i, j$ ) associated with a single aperture measurement. **b** Cartoon of a cross-section of a partially cemented fracture showing multiple aperture measurements associated with a point along the image grid. **c** Exaggerated cartoon of a cross-section of a rough or partially cemented fracture, showing differences in the ‘vertical’ aperture measurement,  $h$ , and the ‘perpendicular’ aperture measurement,  $h_{\perp}$  at points A and B

Fig. 5c, we show a cartoon with exaggerated fracture wall roughness and/or cementation that contains two illustrative points, A and B; for A the perpendicular and vertical aperture are the same, for B the perpendicular aperture is smaller than the vertical aperture. The transmissivity of point A is the product of the cross-sectional area  $wh$  and the permeability associated with  $h$ ,

$$T = kA = \left( \frac{h^2}{12} \right) (wh) = \frac{wh^3}{12}, \quad (6)$$

while for the transmissivity of point B the permeability is now associated with  $h_{\perp}$ ,

$$T = kA = \left( \frac{h_{\perp}^2}{12} \right) (wh) = \frac{wh_{\perp}^2 h}{12}. \quad (7)$$

Therefore, when the total cross-sectional area measured from the aperture measurements,  $A = w \sum_i h_{\alpha}$ , where  $\alpha$  indicates the method of aperture measurement (elaborated on below), is less than the actual total cross-sectional area,  $A = wh_n$ , we apply a cross-sectional area correction,

$$T = kA = \left( \frac{wh_{\alpha}^3}{12} \right) \left( \frac{h_n}{h_{\alpha}} \right). \quad (8)$$

Note that when  $h_{\alpha} = h_n$  Eq. (8) reverts to Eq. (2).

We employ three methods for measuring the aperture distribution. The three local aperture measurement methods are named to reflect the necessary image input to perform the measurement. The ‘vertical’, or 1D aperture,  $h_{1D}$ , is measured as the distance between the fracture walls along the image grid. When multiple apertures can be measured along the image grid the maximum is taken. To determine the ‘perpendicular’ aperture, we employ the Euclidean distance function, which measures the minimum distance to the solid wall for all pore voxels. The 2D aperture,  $h_{2D}$ , is measured by using 2D image slices as the input into the distance function, oriented orthogonal to flow, and is equivalent to fitting a maximum inscribed circle between the fracture walls. The 3D aperture,  $h_{3D}$ , is measured using the 3D image as input into the distance function and is equivalent to fitting a maximum inscribed sphere between the fracture walls. It should be noted that the maximum inscribed sphere aperture measurement is also typically used to measure the pore apertures of porous media, in this way our 3D measurement is ‘viewing’ the fracture as a porous medium, but with a fracture aperture sampling grid. For  $h_{1D}$ ,  $h_{2D}$  and  $h_{3D}$  a measurement is taken at each image grid cell parallel to the fracture plane, resulting in  $wL$  measurements per subsample. The contact fraction,  $C$ , is defined as the number of ‘0’ aperture measurements,  $N_C$ , over the total number of aperture measurements,  $wL$ , and does not vary with choice of aperture measurement. When contact points exist in the fracture pore space the geometric mean of the aperture distribution will be zero. For rough fractures it has been proposed that the statistical moments of the aperture distribution be measured from the open pore space only, while treating the contact fraction as a tortuosity factor (Tsang 1984; Walsh 1981; Zimmerman and Bodvarsson 1996; Zimmerman et al. 1992), as in,

$$h_{A(\alpha)} = \frac{1}{wL - N_C} \sum_{ij} h_{ij(\alpha)}, \quad (9)$$

$$\sigma_{(\alpha)} = \sqrt{\frac{\sum_{i,j,h_{i,j}(\alpha) \neq 0} (h_{i,j}(\alpha) - h_{A(\alpha)})^2}{wL - N_C}}, \quad (10)$$

$$h_{G(\alpha)} = \left( \prod_{i,j,h_{i,j}(\alpha) \neq 0} h_{i,j}(\alpha) \right)^{\frac{1}{wL - N_C}}, \quad (11)$$

where  $\alpha$  indicates the type of aperture measurement (1D, 2D, 3D). Here, we will follow this strategy using the tortuosity factor suggested by Zimmerman and Bodvarsson (1996),  $(1 - 2C)$ . This tortuosity factor treats the contact fraction as being randomly distributed resulting in a percolation threshold of  $C = 0.5$ .

Using fracture transmissivity models that have been reviewed above, with the aperture measurement methodology as proposed here, we compared flow simulation results to the three following fracture permeability models, (1) the ACL using the nominal mean aperture,

$$T_{ACL} = \frac{wh_n^3}{12}, \quad (12)$$

with permeability,

$$k_{ACL} = \frac{h_n^2}{12}, \quad (13)$$

(2) the ACL using the geometric mean aperture (GACL),

$$T_{GACL} = \frac{wh_{G(\alpha)}^3}{12} \frac{h_n}{h_{G(\alpha)}} (1 - 2C), \quad (14)$$

with permeability,

$$k_{GACL} = \frac{h_{G(\alpha)}^2}{12} (1 - 2C), \quad (15)$$

and (3) the Zimmerman and Bodvarsson (1996) model (ZB),

$$T_{ZB} = \frac{wh_{A(\alpha)}^3}{12} \left[ 1 - 1.5 \left( \frac{\sigma_\alpha}{h_{A(\alpha)}} \right)^2 \right] \frac{h_n}{h_{A(\alpha)}} (1 - 2C). \quad (16)$$

with permeability,

$$k_{ZB} = \frac{h_{A(\alpha)}^2}{12} \left[ 1 - 1.5 \left( \frac{\sigma_\alpha}{h_{A(\alpha)}} \right)^2 \right] (1 - 2C). \quad (17)$$

We note that for two rough surfaces, the contact fraction is dependent on the resolution of the aperture measurement, thus, contact is defined as two fracture faces separated by a distance smaller than the resolution of measurement.

## 2.3 Flow Simulation

We directly numerically solve the velocity field of the fracture images for single phase flow using the lattice Boltzmann method (LBM). The fracture walls are treated as impermeable. Flow simulations were conducted using a D3Q19 single-relaxation time LBM, with standard halfway bounce-back (Pan et al. 2006). The open-source code Palabos (Latt 2009) was used to carry out low-resolution simulations and an in-house parallelized LBM code (Landry et al. 2016) was used for higher resolution simulations on high performance computing resources. We translate the segmented images directly into lattices by representing each image voxel with either 1, 8, or 27 lattice nodes. Although it would be optimal to use high-resolution image translation (i.e.  $\geq 27:1$  node:voxel) for all of the flow simulations, the computational demand can become prohibitive. Therefore, we progressively increase the node:voxel ratio for one subsample from each image until the increasing resolution provides fracture permeability measurements within  $\sim 5\%$  of the lower resolution translation. All other fracture subsamples, including those that were digitally dilated larger than the subsample evaluated, were then translated at the lower resolution for flow simulation. We also use the comparison between the 1:1 and 8:1 node:voxel translation results to evaluate the resolution of the images. When critical flow paths are represented by spacing between walls of only one voxel we expect the 1:1 simulations to calculate mean flow velocities that may be upwards of 50% greater than the 8:1 simulations. This expectation derives from the  $1.5\times$  ratio of the maximum to mean velocity of Poiseuille flow between parallel plates. Images with velocity fields that reflect critical flow paths being represented by one voxel wall spacing are considered under-resolved and eliminated from further evaluations. To avoid imposing artificial walls at boundaries parallel to flow, which would artificially decrease the mean velocity solved by the LBM, we mirrored the images parallel to flow to ensure seamless closure of the lattice (infinite fracture width). This results in images with simulation volumes that range from  $440\times 880\times 171$  to  $900\times 1800\times 305\ \delta^3$  (or, for example,  $1800\times 900\times 305\ \delta^3$  when the direction of flow is in the y direction). Pressure boundaries were then imposed at the inlet and outlet layers of the lattice to simulate creeping or laminar flow (Reynold's number  $\ll 1$ ). We do not consider turbulent flow conditions, although it should be noted the LBM is capable of simulating such conditions. We considered turbulent flow—that may occur near wellbores—to be outside the scope of our investigation of flow and mass transport in fractured subsurface rock. From these simulations, the ‘actual’ fracture permeability,  $k_f$ , was determined in accordance with Darcy's law,

$$k_f = \frac{\overline{u_x} \mu L}{\Delta P} \delta^2, \quad (18)$$

where  $\overline{u_x}$  is the mean velocity in the direction of flow,  $\mu$  is the dynamic viscosity (set to  $1/6$  with relaxation time equal to 1), and  $\Delta P$  is the pressure difference across the lattice, all in lattice units. The  $\delta^2$  is a scaling factor that scales the simulation results from lattice units of length to  $\text{m}^2$ . Note that the scaling factor changes with node:voxel translation, for example, an 8:1 translation would have a  $\delta^2$  factor that is  $1/4$  of the 1:1 translation. For each subsample the flow is simulated in both the x and y directions, referred to as X and Y. Note that the 2D aperture measurements are measured orthogonal to the direction of flow, and  $h_{ij}$  may vary depending on orientation of measurement.

### 3 Results

#### 3.1 Aperture Measurements

In Figs. 6 and 7, we show examples of aperture distributions for the rough barren and partially cemented fractures, respectively. For the rough barren fractures, the change in the aperture distribution between the three methods of aperture measurement varies between relatively limited for the rough Berea fracture to more significant for SynFrac C. Of the SynFrac fractures, SynFrac C is the only one composed of surfaces with significant roughness anisotropy, which results in anisotropy in the fracture pore space. For the cement-lined Niobrara fracture the aperture distribution is similar to the Berea fracture, showing only limited variation between the different aperture measurement methods. While both the cement-bridged fractures show a substantial change in aperture distributions depending on the aperture measurement method. The rough barren fractures and SynFrac fractures display normal aperture distributions regardless of the aperture measurement method,

**Fig. 6** Example aperture distributions for rough fractures. **a–e** Synfrac A–E and **f** Berea subsample 1 fracture aperture distributions, showing the 1D (dotted line), 2D (dashed line), and 3D (solid line) aperture distributions

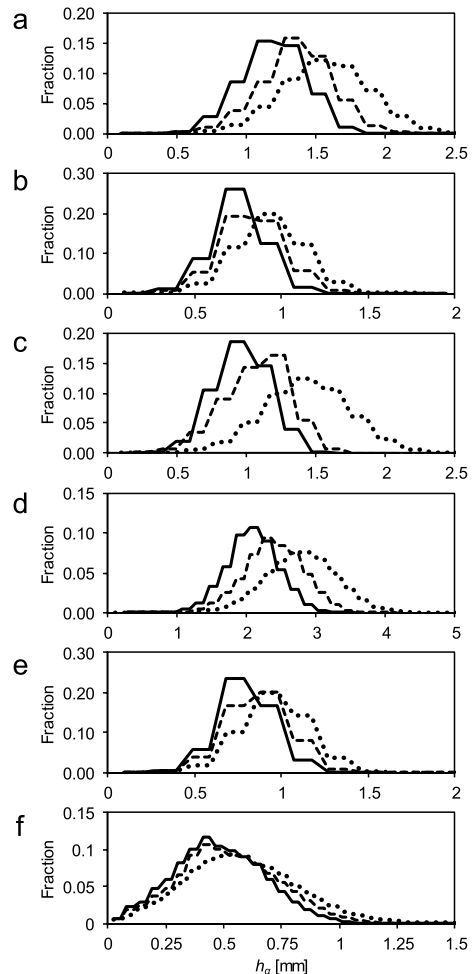
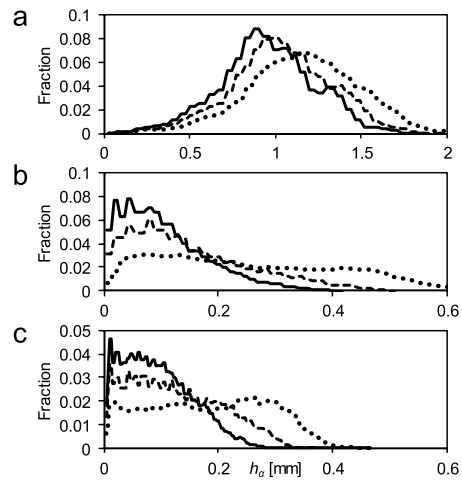




**Fig. 7** Example aperture distributions for partially cemented fractures. **a** Cement-lined Niobrara subsample 1 as imaged, **b** cement-bridged Travis Peak subsample 1, and **c** cement-bridged Mesaverde subsample 1 fracture aperture distributions, showing the 1D (dotted line), 2D (dashed line), and 3D (solid line) aperture distributions



while the Berea fracture aperture distribution tends more towards a lognormal distribution. The Niobrara fracture aperture distribution tends towards a normal distribution, while the cement-bridged fractures show aperture distributions for the perpendicular 2D and 3D aperture measurements that are distinctively lognormal.

### 3.2 Image and Lattice Resolution

The results of the image/lattice resolution evaluation are summarized in Table 2. Only the cement-lined Niobrara fracture image digitally closed by  $-40\delta$  was found to be under-resolved. The Y-direction permeability of subsample 1 and 2 of the  $-40\delta$  digitally closed Niobrara fracture image had 48.79 and 42.33%  $k_f$  overestimates between the 1:1 and 8:1 node:voxel translations, respectively. These  $k_f$  overestimates approach 50%, which is indicative of under-resolved images for flow simulation. Although the X-direction  $k_f$  for these subsamples is found to be well-resolved—a result of the strong fracture permeability anisotropy to be further discussed below—we eliminated the  $-40\delta$  digitally closed fracture image from further analysis. The  $-30\delta$  digitally closed Niobrara fracture image was found to have a relatively small %  $k_f$  overestimates between the 1:1 and 8:1 node:voxel translations and was considered well-resolved. The  $-20$  to  $+100\delta$  digitally closed/opened Niobrara fracture images are deemed well-resolved by the fact that the mean fracture to voxel size ratio is larger than the  $-30\delta$  digitally closed image. All other fracture images showed relatively small ( $<13\%$ )  $k_f$  overestimates between the 1:1 and 8:1 node:voxel translations and were considered well-resolved.

Although most of the fracture images were found to be well-resolved we are also interested in ensuring the velocity fields are well-resolved, as in, to minimize ( $<5\%$ ) the error in the measured  $k_f$  as a result of discretization errors. For subsample 1 of the as imaged ( $0\delta$ ) Berea fracture the difference between the measured  $k_f$  of the 1:1 and 8:1 node:voxel translation was 4.51%, therefore performing simulations at 1:1 can be expected to produce overestimates of approximately  $<5\%$ . For the Berea fracture subsamples all other LBM simulations used a 1:1 node:voxel translation. For subsample 1 of the  $-30\delta$  digitally closed Niobrara fracture the Y-direction  $k_f$  the 1:1 node:voxel shows an overestimate 11.00%, therefore the  $k_f$  in the Y-direction for the  $-30\delta$  digitally closed Niobrara

**Table 2** Summary of image/lattice resolution evaluation

Fracture (subsample number, open/close [ $\delta$ ])	Flow direction	1:1 $k_f$ [D]	1:8 $k_f$ [D]	% $k_f$ Overestimate 1:1 vs. 8:1 [node:voxel]	1:27 $k_f$ [D]	% $k_f$ Overestimate 8:1 versus 27:1 [node:voxel]
Berea	X	9891	9464	<b>4.51</b>	—	—
(1, 0)	Y	20,680	—	—	—	—
Niobrara	X	614.1	550.1	11.63	—	—
(1, -40)	Y	128.9	86.63	<b>48.79</b>	—	—
Niobrara	X	1859	1772	4.91	—	—
(2, -40)	Y	569.6	400.2	<b>42.33</b>	—	—
Niobrara	X	5219	4999	<b>4.40</b>	—	—
(1, -30)	Y	3037	2736	11.00	—	—
SynFrac A	X	106,000	97,690	8.51	95,020	<b>2.81</b>
(1, 0)	Y	105,400	97,100	8.55	—	—
SynFrac B	X	42,140	37,750	11.63	36,330	<b>3.91</b>
(1, 0)	Y	42,590	38,160	11.61	—	—
SynFrac C	X	67,920	60,620	12.04	58,350	<b>3.89</b>
(1, 0)	Y	60,990	54,030	12.88	—	—
SynFrac D	X	350,700	332,300	<b>5.54</b>	—	—
(1, 0)	Y	351,700	—	—	—	—
SynFrac E	X	49,140	44,710	9.91	43,270	<b>3.33</b>
(1, 0)	Y	48,300	44,500	8.54	—	—
Travis Peak	X	19.23	18.07	<b>6.42</b>	—	—
(1, 0)	Y	25.11	—	—	—	—
Mesaverde	X	187.0	184.2	<b>1.52</b>	—	—
(2, 0)	Y	256.4	—	—	—	—

fracture was measured using an 8:1 node:voxel translation. For subsample 1 of the  $-30$   $\delta$  digitally closed Niobrara fracture the difference between the measured  $k_f$  of the 1:1 and 8:1 node:voxel translation was 4.40%, for the X-direction  $k_f$  of the  $-30$  digitally closed Niobrara fracture and all other LBM simulations for the Niobrara fracture were performed with a 1:1 voxel:node translation. For the SynFrac A, B, C, and E fractures the difference between the measured  $k_f$  of the 1:1 and 8:1 node:voxel translation was between 8.51 and 12.88%. To ensure the 8:1 node:voxel translations for the SynFrac fractures were small 27:1 node:voxel translation lattices were also ran and showed the difference between the measured  $k_f$  of the 8:1 and 27:1 node:voxel translation were between 2.81 and 3.89%. All SynFrac LBM simulations in the Y-direction used an 8:1 node:voxel translation for measurement of  $k_f$ , except for SynFrac D which used a 1:1 node:voxel translation, as justified by the small difference between the measured  $k_f$  of the 1:1 and 8:1 node:voxel translation in the X-direction. For subsample 1 of the Travis Peak fracture the difference between the measured  $k_f$  of the 1:1 and 8:1 node:voxel translation was 6.43%. This is greater than the  $\sim 5\%$  overestimate target, however, the 8:1 Travis Peak simulation required 4.81 CPU\*years to converge, which is a high computational demand. Therefore, we chose to run the rest of the Travis Peak subsample LBM simulations with a 1:1 translation. For subsample 1 of the Mesaverde fracture the difference between the measured  $k_f$  of the 1:1 and 8:1 node:voxel translation was 1.52%, and all other Mesaverde fracture subsample LBM simulations used a 1:1 node:voxel translation. Note, that where available from the discretization error evaluation the higher resolution node:voxel translations LBM simulation  $k_f$  was used in further analysis below.

### 3.3 Fracture Permeability Model Estimates versus Measurements

The fracture permeability for all fracture subsamples varies over 6 orders of magnitude (Fig. 8a). In Fig. 8, we also include the results of Gale et al. (1990) and Hakami (1989) compiled in Zimmerman and Bodvarsson (1996) and from Konzuk and Kueper (2004), for rough barren fractures in granite and limestone, respectively. These physical measurements of permeability give similar results to those here. The ACL model informed by the nominal mean aperture does not include any aperture distribution information but is equal to the arithmetic mean when the contact fraction is minimal. As would be expected,  $k_f$  is consistently less than that predicted by the ACL. In general, the discrepancy between  $k_f$  and  $k_{ACL}$  increases with increasing relative roughness,  $\sigma_{1D}/h_{A(1D)}$ , and contact fraction,  $C$  (Fig. 8a–c). The model-actual ratio,  $k_{ACL}/k_f$ , varies from 1.14 for the digitally opened rough Berea fracture and the digitally opened cement-lined Niobrara fracture to between 8 and 85 for the cement-bridged fractures (Fig. 8d). All fracture types, when including those compiled in Zimmerman and Bodvarsson (1996), approach order of magnitude overestimates at high relative roughness. There are two model-actual ratios that deviate significantly from the rest of the dataset at lower relative roughness, these are SynFrac C in the X and Y directions.

In Fig. 9, we present the model-actual ratio for the ACL using the geometric mean aperture ( $GACL$ ),  $k_{G(\alpha)}/k_f$ , and ZB fracture permeability model,  $k_{ZB(\alpha)}/k_f$ , as a function of relative roughness for the three aperture measurement types. Note that the physical measurements of fracture permeability compiled in Zimmerman and Bodvarsson (1996) only included 1D aperture measurements. Overall, the use of either model improves the accuracy of fracture permeability estimates over the ACL informed by the nominal mean aperture. For the 1D aperture measurement, the fracture permeability is overestimated

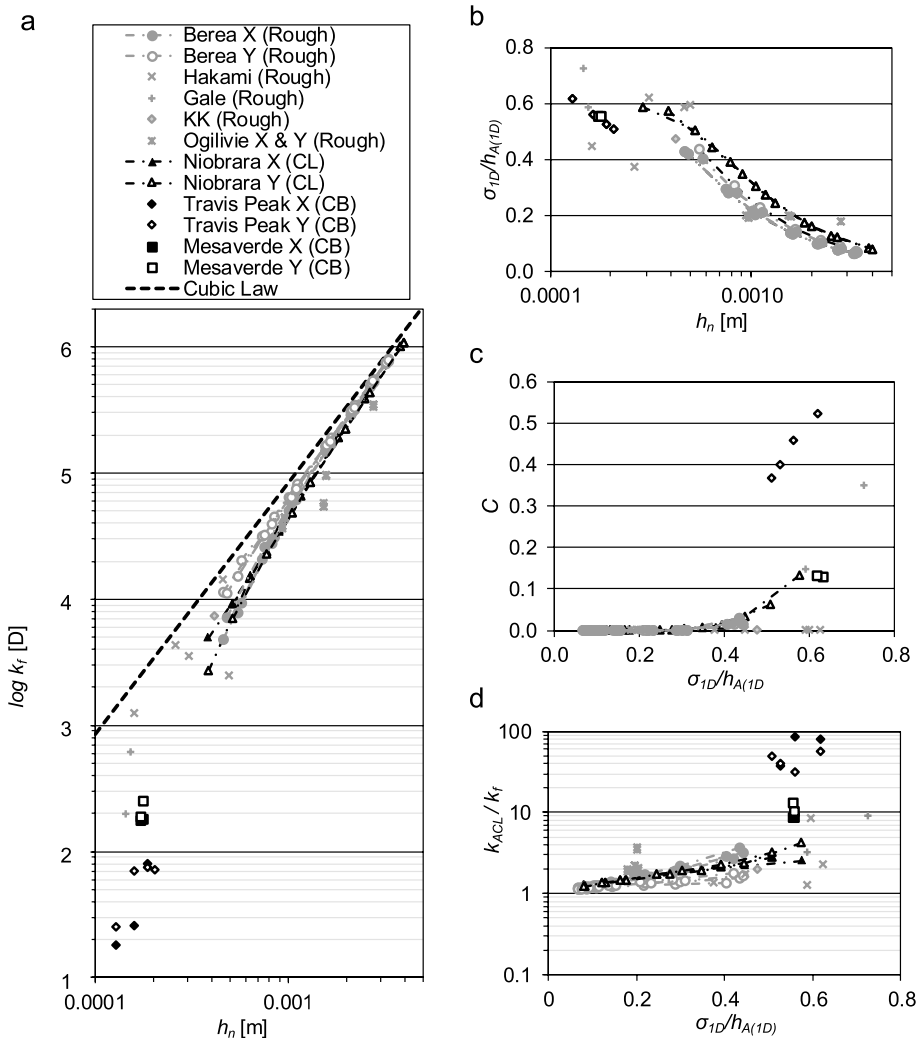


**Fig. 8** Fracture permeability, relative roughness, contact fraction, and model-actual ratio for the alternative cubic law. **a** Fracture permeability,  $k_f$ , determined by LB simulations as a function of nominal mean aperture,  $h_n$ , including physical measurements of fracture permeability taken from the literature (Hakami 1989 (Hakami), Gale et al. 1990 (Gale), Konzuk and Kueper 2004 (KK), SynFracs of Ogilvie et al. 2006 (Ogilvie)), with fracture type—rough barren (Barren), cement-lined (CL), cement-bridged (CB)—indicated in the legend. **b** 1D relative roughness,  $\sigma_{1D}/h_{1D}$ , as a function of nominal mean aperture  $h_n$ . **c** Contact fraction,  $C$ , as a function of 1D relative roughness, note that the 2D and 3D relative roughness differs from the 1D, but are similar in value and follow the same trends as shown in (b, c). **d** Model-actual ratio,  $k_{ACL}/k_f$ , for the alternative cubic law as a function of 1D relative roughness

for nearly all the measurements made here. There are two rough barren fracture estimates from the (Hakami 1989) measurements that show underestimates for the GACL and ZB models which can likely be attributed to the limited aperture measurement methodology of Hakami (1989). These underestimates are exceptions, the cement-bridged fracture permeability was overestimated by over an order of magnitude. For the rough barren fractures

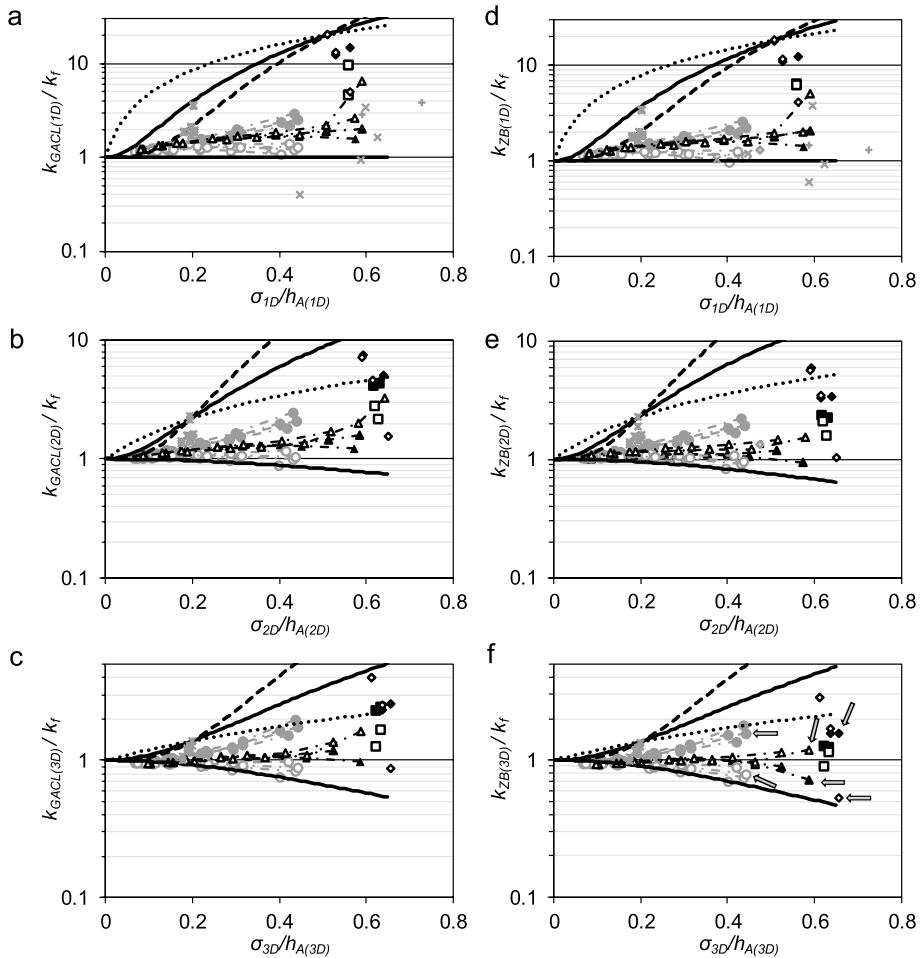


**Fig. 9** Model-actual ratio for the GACL and ZB fracture permeability models for all subsamples. **a–c** Model-actual ratio,  $k_{G(a)}/k_f$ , for GACL fracture permeability model, and **d–f** model-actual ratio,  $k_{ZB(a)}/k_f$ , for ZB fracture permeability model. Symbols same as in Fig. 8, dotted, solid, and dashed lines represent Eq. (19) with  $\gamma$  set to 1, 2, and 3, respectively, fitted to results. The arrows in (f) indicate the simulations visualized in Fig. 10.

the permeability is overestimated by upwards of a factor of 3, with SynFrac C model-actual ratios again deviating from those of the other rough barren fractures at the same relative roughness. The GACL and ZB model estimates using the 1D aperture measurements are an improvement over the estimates using the ACL, but for the partially cemented fractures the estimates are still relatively poor. The improvement in the estimates using the 2D aperture measurement over the 1D aperture measurement is significant for all the fractures and both models. For the 2D aperture measurements, the rough barren fracture estimates vary from being slightly underestimated to overestimated by approximately a factor of 2. For the partially cemented fractures the overestimates drop to a factor of 8 and 6, and less, for the GACL and ZB models, respectively. For the 3D aperture measurements, the improvement over the estimates using the 2D aperture measurements for the rough barren fractures is

limited, but the overestimate of SynFrac C is no longer significantly greater than that of the other SynFrac fractures. Notably, the model-actual ratios for the SynFrac fractures are very similar although their permeability and statistical properties vary significantly. The overestimate of the rough barren Berea fracture in the X direction and underestimation in the Y direction can be attributed to the bedding, which runs roughly parallel to the Y direction. The fracture permeability estimates for the cement-bridged fractures significantly improve using the 3D aperture measurement, with a range from an underestimate by a factor of ~1.6 (note: coincides with a model-actual ratio of ~0.63) to an overestimate of ~3 for the Travis Peak fractures. The ZB fracture permeability model-actual ratios for the Mesaverde cement-bridged fractures are much smaller than those for the Travis Peak fracture, which is likely due to their smaller contact fraction in comparison to the Travis Peak fractures. Overall, the accuracy for the two models is very similar regardless of the aperture measurement method, with the ZB model providing slightly more accurate estimates for both rough and partially cemented fractures.

One of the cement-bridged fractures of the Travis Peak subsamples was found to have a contact fraction of 0.523 yet contained a connected fracture pore space across the subsample volume. This contact fraction is outside of the prediction limits of the fracture tortuosity factor,  $1 - 2C$ , which assumes a percolation limit with a contact fraction of 0.5. This contact fraction percolation limit is only an average derived by assuming that local contact points are randomly distributed within a finite fracture volume. When only a limited portion of a fracture is evaluated, as was done here, there is a significant possibility for any spatial arrangement to be non-percolating or percolating, below or above a contact fraction of 0.5, respectively. Essentially, we argue that this result does not show the fracture tortuosity factor as an ineffective correlation, but rather reflects the limited sampling size of the XCMT images.

Notably, all of the results converge at model-actual ratios of approximately 1 as a function of decreasing relative roughness. Although our results used portions of fractures that were limited in spatial extent due to limitations in XCMT technology the spread of the model-actual ratios is similar for fractures independent of host rock lithology and form of cementation (lining vs. bridging cement). This suggests that an upper and lower boundary of fracture permeability estimates can be defined for all fractures evaluated here. To define the upper and lower bounds of the fracture permeability model estimates, we employ a simple empirical function first used by Méheust and Schmittbuhl (2001), albeit with a different goal, to describe the upper,  $k_U = Fk_M$ , and lower,  $k_L = F^{-1}k_M$ , bounds where  $k_M$  is the fracture permeability model estimate and  $F$  is a function of the relative roughness,

$$F = 1 + \beta \left( \frac{\sigma_\alpha}{h_{A(\alpha)}} \right)^\gamma, \quad (19)$$

where  $\beta$  is fitted to the results such that all measurements fall approximately—with a tolerance of  $(k_{M(\alpha)}/k_f) = \pm 0.02$  to avoid the bounds being defined by small fluctuations in the model-actual ratio at low relative roughness—within the upper and lower limit bounds (not including results compiled in Zimmerman and Bodvarsson (1996) for the 1D aperture measurement), with  $\gamma$  values of, 1, 2, and 3. In Fig. 9, we show the upper bound of Eq. (19) fitted for  $\gamma$  values of 1, 2, and 3. It is apparent in Fig. 9 that a value of 2 for  $\gamma$  most consistently captures the model-actual ratios. A  $\gamma$  value of 1 overestimates the upper bound at lower relative roughness and underestimates the upper bound at higher relative roughness. In contrast, a  $\gamma$  value of 3 underestimates the upper bound at lower relative roughness and overestimates the upper bound at higher relative roughness. Therefore, we suggest that



Eq. (19) be simplified to setting the value of  $\gamma$  to 2, while fitting values of  $\beta$  for the GACL and ZB models as summarized in Table 3.

In Fig. 10, we show examples of 3D aperture maps and velocity field renderings for flow simulations with the highest relative roughness for the rough barren, cement-lined, and cement-bridged fractures. The Berea rough barren fracture aperture map shows a clear anisotropy that correlates with bedding. This anisotropy is reflected in the flow, with flow perpendicular to bedding (X) being significantly less than flow parallel to bedding (Y) (Fig. 10a). The flow parallel to the bedding is higher because the flow paths are less tortuous and not forced through the smaller apertures. It has previously been established that a decrease in flow rates for fractures correlates with increasing flow channelling (Brown 1987; Glover et al. 1997; Tsang 1984). The aperture map for the Niobrara cement-lined fracture after  $-30 \delta$  digital closure shows significant portion of the right hand side of the subsample is closed. This pattern is expected near the edge of fractures where the kinematic aperture drops to 0, or the volume becomes completely in-filled with cement. The cement-lined and cement-bridged fracture aperture maps do not show readily distinguishable anisotropy, but the flow in the X and Y directions are significantly different (Fig. 10b). The ZB model underestimates the fracture permeability for the cement-lined fracture shown in Fig. 10b by a factor of 1.388 (model-actual ratio of 0.7205) when flowing in the X direction, which can be attributed to most of the flow occurring along a straight path at the bottom of the subsample. While in the Y direction, the flow is more tortuous and forced through small apertures leading to overestimation. For the Travis Peak cement-bridged fracture subsample, the flow in the X direction is overestimated by a factor of 1.567, while the flow in the Y direction is underestimated by a factor of 1.855 (Fig. 10c). The differences in flow between the X and Y directions for the cement-bridged fracture can be attributed to the same factors as observed in the cement-lined fracture, with more tortuous flow in the X direction.

The flow patterns observed in the partially cemented fractures are similar to what is observed in the rough fracture, however, for the partially cemented fractures the spatial arrangement of apertures is driven by precipitation processes. While the anisotropy in the rough barren fracture can be expected to persist for larger fracture volumes than what was imaged here, the same may not be expected for the partially cemented fractures. The image sizes are determined by the technological limitations of XCMT. Theoretically, for an isotropic rough barren fracture in a matrix with homogenous mineralogic composition, any subsequent accumulation of cement lining or cement bridging would result in an isotropic morphology and topology. It is possible that the anisotropy we observe in the partially cemented fractures imaged here is a result of the limited sample size. If we assume that the anisotropy observed in the partially cemented fractures imaged here is due to the limited sample size, then it is arguable that a more representative measure of the

**Table 3** Fitted  $\beta$  values for Eq. (19)

Fracture model (aperture measurement type)	$\beta_L$	$\beta_U$
$k_{\text{GACL}(1\text{D})}$	0.0	74.1
$k_{\text{ZB}(1\text{D})}$	7.19e-3	67.6
$k_{\text{GACL}(2\text{D})}$	0.806	30.9
$k_{\text{ZB}(2\text{D})}$	1.33	33.16
$k_{\text{GACL}(3\text{D})}$	2.04	9.68
$k_{\text{ZB}(3\text{D})}$	2.65	8.96

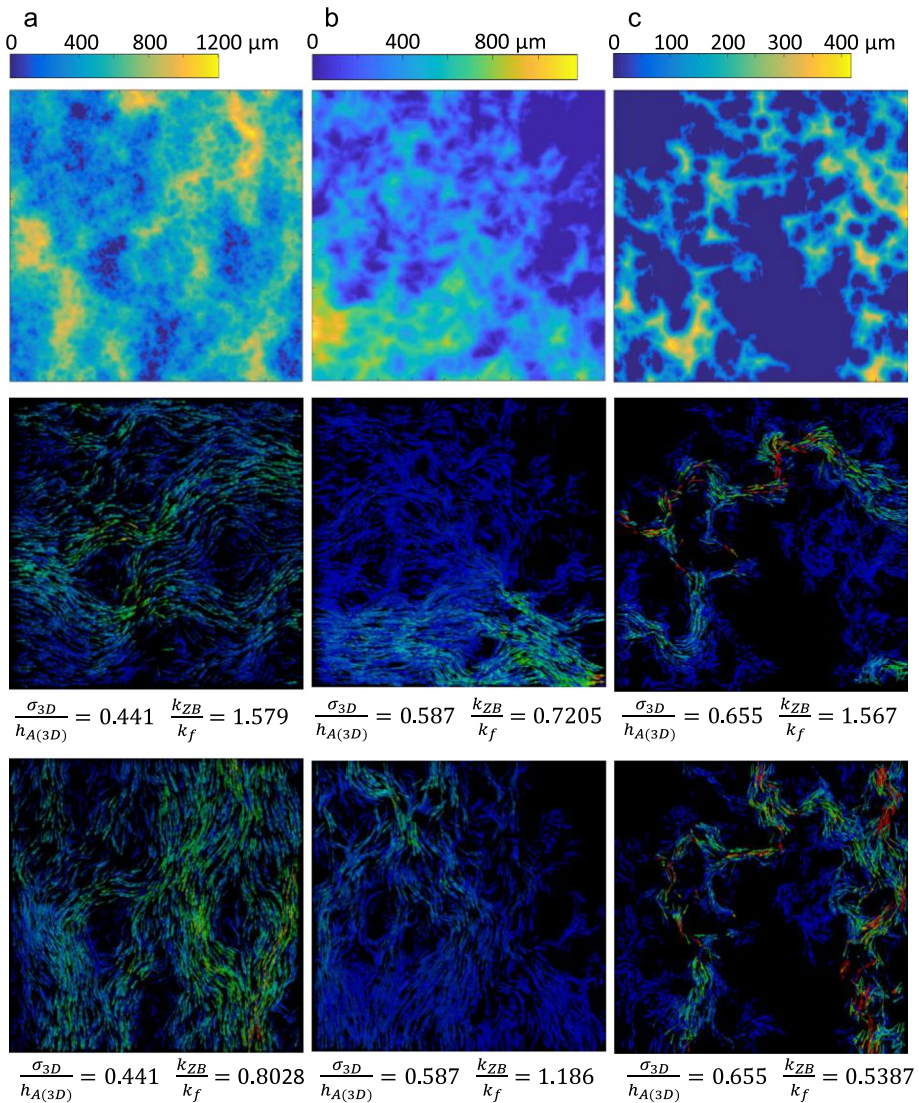


**Fig. 10** 3D aperture maps and LBM velocity field examples. 3D aperture map (top) and velocity fields for flow in the X (middle) and Y (bottom) directions for **a** Berea rough fracture, **b** Niobrara cement-lined fracture, and **c** Travis Peak cement-bridged fracture subsamples. Above the velocity field renderings, the relative roughness and model-actual ratio for the ZB model are given. For the velocity fields, the glyph colour is scaled to the velocity magnitude with blue to red colouring indicating lower and higher velocities, respectively

fracture permeability would be the average permeability for all flow directions, which we can estimate by taking the average from the flow simulations in the X and Y directions,  $k_f = (k_{fX} + k_{fY})/2$ . When we assume the partially cemented fractures are isotropic and take the actual fracture permeability as the average of the fracture permeability in the X and Y directions the ZB fracture permeability model no longer shows underestimation of

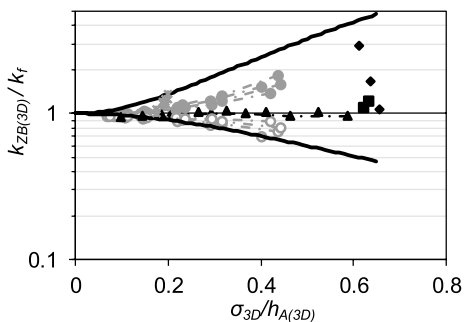
flow (Fig. 11). This interpretation of the partially cemented fracture permeability does not change the  $\beta$  values because they were determined by the model-actual ratio of SynFrac C to ensure all measurements fall below the upper bound limit. A summary of all aperture measurements, model estimates, measured fracture permeability, and model-actual ratios are provided in supporting information Tables S1–S3.

## 4 Discussion

The deviations from the fracture permeability model estimates observed here have been previously attributed to the tortuosity of flow paths (e.g. Tsang 1984). This tortuosity is only partially captured by the contact fraction tortuosity factor, which approximates the tortuosity due to contact areas in a smooth flat fracture. The aperture spatial arrangement also contributes to the tortuosity (Brown 1987; Tsang 1984), however, when only the aperture distribution is known, it is not possible to correct for this. Which is one of the motivations for establishing upper and lower bounds on fracture permeability estimates. Better estimates could be developed if the spatial arrangement of the apertures was considered and correlations between permeability and aperture distribution allowed for fitted parameters (Chen et al. 2017; Foroughi et al. 2018; Huang et al. 2017), but this could come at a cost of generality. Note that we are differentiating between spatial correlations related to the aperture and spatial correlations related to rough fracture surfaces (e.g. Brown and Scholz 1985). The latter has a minimal impact on the deviation of fracture permeability estimates from the actual fracture permeability as demonstrated by our SynFrac fracture results and previously reported for other digitally synthesized fractures (e.g. Brown 1987; Méheust and Schmittbuhl 2001). The utility of developing a general fracture permeability model that includes spatial correlation information remains unclear, particularly for partially cemented fractures.

The model-actual ratios for the alternate cubic law (ACL) informed by the nominal mean aperture are relatively small for the rough and cement-lined fractures when the relative roughness is small ( $< 0.1$ ), but becomes significant with increasing relative roughness, reaching overestimates of one to two orders of magnitude for all fracture types considered. This suggests that flow can be well-described with only knowledge of the nominal mean aperture when the relative roughness of the fractures dominating flow is small. But when relative roughness is greater than  $\sim 0.3$  the ACL overestimates flow by a factor of 2 and upwards of a factor of 4.5 for the cement-lined fractures. Implying that the porosity–permeability relationships employed in coupled hydro-chemical fractured rock flow

**Fig. 11** Model-actual ratio for the ZB fracture permeability model assuming partially cemented fractures are isotropic. Note that the symbols representing the partially cemented fractures (black) now represent the mean directional fracture permeability,  $k_f = (k_{fX} + k_{fY})/2$ , not the fracture permeability in  $X$  direction



simulations which relate fracture permeability to volume reductions from precipitation as function of the nominal mean aperture (e.g. Chaudhuri et al. 2012; Verma and Pruess 1988) may underestimate the reduction in flow resulting from precipitation. For fractures with cement bridges, the underestimate in reduction in flow resulting from precipitation may be far more severe. Including the first two moments of the open pore space aperture distribution and the contact fraction in fracture permeability models greatly improves the accuracy of fracture permeability estimates. The local velocity in any pore space is roughly a function of its distance from the pore wall, so it is unsurprising the 3D aperture measurement provides the most accurate fracture permeability estimates. Considering the complexity of the pore spaces in the digitally closed cement-lined fractures and the cement-bridged fractures it is somewhat surprising that the fracture permeability estimates given by the GACL and ZB models are accurate within a factor of  $\sim 3$ . It is apparent that correlating permeability reduction in fractures as a result of precipitation may be substantially improved with the inclusion of the aperture distribution moments. However, it should be noted that the utility of coupling dissolution and transport processes using the statistical moments of the aperture distribution remains unclear. During dissolution, it is possible for wormholes and highly localized flow channels to develop (e.g. Deng et al. 2015; Ellis and Peters 2016) that may be dissimilar to the pore space morphology and topology created by cement precipitation investigated here.

The empirical characterizations developed here (i.e. Eq. (19)) are subject to the limited number of physical fractures we can evaluate, and there are certainly fractures that can be theorized with fracture permeability and aperture distribution relationships that may deviate from those shown here. Studies on natural fractures in oil and gas reservoirs (Brown 1995; Gale et al. 2010, 2014; Ogilvie et al. 2006) demonstrate that the fractures chosen for this study are similar to those commonly encountered. The robustness of our results is dependent on how representative the variety of fracture pore spaces investigated are of fracture pore spaces encountered in a wide range of geological settings. The upper and lower bounds described by Eq. (19) will remain subject to revision, but they provide an initial quantification of fracture permeability estimates established using images of real fractures.

## 5 Conclusions

We have presented an analysis of fracture permeability model estimates from aperture distributions for a rough barren artificial fracture, five digitally synthesized rough barren fractures, a cement-lined natural fracture, and two cement-bridged natural fractures using a digital rock physics workflow. Aperture distributions were measured from segmented three-dimensional XCMT images of the fractures, and digitally synthesized rough fractures. The method of local aperture measurement for 'real' rough barren and partially cemented fractures was addressed and three aperture measurement methods proposed and evaluated. We also proposed a 'cross-sectional area correction' defined by the fracture pore volume for relating transmissivity and fracture permeability to be used when the morphology and topology of the fracture pore space deviates from the theoretical description of rough fractures as two rough surfaces. The fracture permeability was estimated from three models, the alternative cubic law (ACL) using the nominal mean aperture, the alternate cubic law using the geometric mean and a contact fraction tortuosity factor (GACL), and the Zimmerman and Bodvarsson (1996) fracture

permeability model (ZB). The fracture permeability predicted by the models was then compared to the actual fracture permeability determined by lattice Boltzmann model fluid flow simulations.

We found the ACL overestimated fracture permeability by upwards of one order of magnitude for the rough barren and cement-lined fractures, and upwards of two orders of magnitude for the cement-bridged fractures. When the relative roughness is less than 0.1 the model-actual ratios for the ACL were small, with overestimates less than a factor of 1.3, but grew significantly larger at higher relative roughness. This suggests that the porosity–permeability relationships employed in coupled hydro-chemical fractured rock flow simulations which relate fracture permeability to volume reductions from precipitation as function of the nominal mean aperture may underestimate the reduction in flow resulting from precipitation. Including the first two moments of the open pore space aperture distribution and the contact fraction in the fracture permeability estimates of the GACL and ZB models substantially decreased the model-actual ratios, with the best estimates being given using the 3D aperture measurement. The difference between the GACL and ZB model estimates was small with the ZB model providing slightly better estimates. For the partially cemented fractures, the accuracy of estimates using the ZB model were similar to those for the rough barren fractures. In other words, although the fracture pore space morphology and topology of the partially cemented fractures are distinctive from those observed in rough barren fractures, the models developed to correlate fracture permeability and fracture geometry for rough barren fractures are also useful for partially cemented fractures. Finally, we fit an empirical function (Eq. 19) to define the upper and lower bounds on fracture permeability estimates which can be used to assign fracture permeability in explicit fracture representation numerical simulations of flow and mass transport in fractured rock for both rough barren and partially cemented fractures.

**Supplementary Information** The online version contains supplementary material available at <https://doi.org/10.1007/s11242-024-02059-y>.

**Acknowledgements** This research was supported by Saudi Aramco, NSF EarthCube grant 1541008, and a seed grant from the Jackson School of Sciences, The University of Texas at Austin. The authors acknowledge the Texas Advanced Computing Center (TACC) at The University of Texas at Austin for providing high performance computing (HPC) resources. The input imaged data for most of the fractures in this work is published on Digital Rocks Portal, and the derivative work can be obtained by contacting the corresponding author. Exxon Mobil is gratefully acknowledged for the Mesaverde tight sandstone sample.

**Author Contributions** All authors contributed to the study conception and design. Material preparation, data collection, and analysis were performed by CJL. The first draft of the manuscript was written by CJL, and all authors commented on previous versions of the manuscript. All authors read and approved the final manuscript.

**Funding** This research was supported by Saudi Aramco, NSF EarthCube Grant 1541008, and a seed grant from the Jackson School of Sciences, The University of Texas at Austin. The authors acknowledge the Texas Advanced Computing Center (TACC) at The University of Texas at Austin for providing high performance computing (HPC) resources.

**Data Availability** The input imaged data for most of the fractures in this work is published on Digital Rocks Portal, and the derivative work can be obtained by contacting the corresponding author.

## Declarations

**Conflict to interest** The authors have no relevant financial or non-financial interests to disclose.



## References

- Becker, S.P., Eichhubl, P., Laubach, S.E., Reed, R.M., Lander, R.H., Bodnar, R.J.: A 48 m.y. history of fracture opening, temperature, and fluid pressure: Cretaceous Travis Peak Formation, East Texas basin. *Geol. Soc. Am. Bull.* **122**(7–8), 1081–1093 (2010). <https://doi.org/10.1130/B30067.1>
- Belayneh, M.W., Matthai, S.K., Blunt, M.J., Rogers, S.F.: Comparison of deterministic with stochastic fracture models in water-flooding numerical simulations. *AAPG Bull.* **93**(11), 1633–1648 (2009). <https://doi.org/10.1306/07220909031>
- Bisdom, K., Gauthier, B.D.M., Bertotti, G., Hardebol, N.J.: Calibrating discrete fracture-network models with a carbonate three-dimensional outcrop fracture network: implications for naturally fractured reservoir modeling. *AAPG Bull.* **98**(7), 1351–1376 (2014). <https://doi.org/10.1306/02031413060>
- Borgia, A., Pruess, K., Kneafsey, T.J., Oldenburg, C.M., Pan, L.: Numerical simulation of salt precipitation in the fractures of a CO<sub>2</sub>-enhanced geothermal system. *Geothermics* **44**, 13–22 (2012). <https://doi.org/10.1016/j.geothermics.2012.06.002>
- Brown, S.R.: Fluid flow through rock joints: the effect of surface roughness. *J. Geophys. Res.* **92**(B2), 1337–1347 (1987)
- Brown, S.R.: Simple mathematical model of a rough fracture. *J. Geophys. Res. Solid Earth* **100**(B4), 5941–5952 (1995). <https://doi.org/10.1029/94JB03262>
- Brown, S.R., Scholz, C.H.: Broad bandwidth study of the topography of natural rock surfaces. *J. Geophys. Res. Solid Earth* **90**(B14), 12575–12582 (1985). <https://doi.org/10.1029/JB090iB14p12575>
- Cao, P., Karpyn, Z.T., Li, L.: Self-healing of cement fractures under dynamic flow of CO<sub>2</sub>-rich brine. *Water Resour. Res.* **51**(6), 4684–4701 (2015). <https://doi.org/10.1002/2014WR016162>
- Chaudhuri, A., Rajaram, H., Viswanathan, H.: Fracture alteration by precipitation resulting from thermal gradients: upscaled mean aperture-effective transmissivity relationship. *Water Resour. Res.* **48**(1), W01601 (2012). <https://doi.org/10.1029/2011WR010983>
- Chen, Y., Liang, W., Lian, H., Yang, J., Nguyen, V.P.: Experimental study on the effect of fracture geometric characteristics on the permeability in deformable rough-walled fractures. *Int. J. Rock Mech. Min. Sci.* **98**, 121–140 (2017). <https://doi.org/10.1016/j.ijrmm.2017.07.003>
- Cvetkovic, V., Frampton, A.: Solute transport and retention in three-dimensional fracture networks. *Water Resour. Res.* **48**(2), W02509 (2012). <https://doi.org/10.1029/2011WR011086>
- Dagan, G.: Models of groundwater flow in statistically homogeneous porous formations. *Water Resour. Res.* **15**(1), 47–63 (1979). <https://doi.org/10.1029/WR015i001p00047>
- Dahi Taleghani, A., Olson, J.E.: How natural fractures could affect hydraulic-fracture geometry. *SPE J.* **19**(01), 161–171 (2014). <https://doi.org/10.2118/167608-PA>
- de Dreuzy, J.-R., Méheust, Y., Pichot, G.: Influence of fracture scale heterogeneity on the flow properties of three-dimensional discrete fracture networks (DFN): 3D fracture network permeability. *J. Geophys. Res. Solid Earth* (2012). <https://doi.org/10.1029/2012JB009461>
- Deng, H., Fitts, J.P., Crandall, D., McIntyre, D., Peters, C.A.: Alterations of fractures in carbonate rocks by CO<sub>2</sub>-acidified brines. *Environ. Sci. Technol.* **49**(16), 10226–10234 (2015). <https://doi.org/10.1021/acs.est.5b01980>
- Ebigbo, A., Lang, P.S., Paluszny, A., Zimmerman, R.W.: Inclusion-based effective medium models for the permeability of a 3D fractured rock mass. *Transp. Porous Media* **113**(1), 137–158 (2016). <https://doi.org/10.1007/s11242-016-0685-z>
- Ellis, B.R., Peters, C.A.: 3D Mapping of calcite and a demonstration of its relevance to permeability evolution in reactive fractures. *Adv. Water Resour.* **95**, 246–253 (2016). <https://doi.org/10.1016/j.advwatres.2015.07.023>
- Fall, A., Eichhubl, P., Cumella, S.P., Bodnar, R.J., Laubach, S.E., Becker, S.P.: Testing the basin-centered gas accumulation model using fluid inclusion observations: Southern Piceance Basin, Colorado. *AAPG Bull.* **96**(12), 2297–2318 (2012). <https://doi.org/10.1306/05171211149>
- Fall, A., Eichhubl, P., Bodnar, R.J., Laubach, S.E., Davis, J.S.: Natural hydraulic fracturing of tight-gas sandstone reservoirs, Piceance Basin, Colorado. *Geol. Soc. Am. Bull.* **B31021**, 1 (2014). <https://doi.org/10.1130/B31021.1>
- Foroughi, S., Jamshidi, S., Pishvaie, M.R.: New correlative models to improve prediction of fracture permeability and inertial resistance coefficient. *Transp. Porous Media* (2018). <https://doi.org/10.1007/s11242-017-0930-0>
- Fu, P., Johnson, S.M., Carrigan, C.R.: An explicitly coupled hydro-geomechanical model for simulating hydraulic fracturing in arbitrary discrete fracture networks: fully coupled model for hydro-fracturing in arbitrary fracture networks. *Int. J. Numer. Anal. Methods Geomech.* **37**(14), 2278–2300 (2013). <https://doi.org/10.1002/nag.2135>



- Gale, J.F.W., Lander, R.H., Reed, R.M., Laubach, S.E.: Modeling fracture porosity evolution in dolostone. *J. Struct. Geol.* **32**(9), 1201–1211 (2010). <https://doi.org/10.1016/j.jsg.2009.04.018>
- Gale, J.F.W., Laubach, S.E., Olson, J.E., Eichhuble, P., Fall, A.: Natural fractures in shale: a review and new observations. *AAPG Bull.* **98**(11), 2165–2216 (2014). <https://doi.org/10.1306/08121413151>
- Gale, J., MacLeod, R., LeMessurier, P.: Site characterization and validation-Measurement of flowrate, solute velocities and aperture variation in natural fractures as a function of normal and shear stress, stage 3. Swedish Nuclear Fuel and Waste Management Co (1990). [https://inis.iaea.org/search/search.aspx?orig\\_q=RN:22037162](https://inis.iaea.org/search/search.aspx?orig_q=RN:22037162)
- Geiger, S., Matthai, S.: What can we learn from high-resolution numerical simulations of single- and multi-phase fluid flow in fractured outcrop analogues? *Geol. Soc. Lond. Spec. Publ.* **374**(1), 125–144 (2014). <https://doi.org/10.1144/SP374.8>
- Glover, P.W.J., Matsuki, K., Hikima, R., Hayashi, K.: Fluid flow in fractally rough synthetic fractures. *Geophys. Res. Lett.* **24**(14), 1803–1806 (1997). <https://doi.org/10.1029/97GL01670>
- Hakami, E.: Water flow in single rock joints (Licentiate Thesis). Lulea University of Technology, Lulea, Sweden (1989). [http://www.iaea.org/inis/collection/NCLCollectionStore/\\_Public/21/042/21042656.pdf](http://www.iaea.org/inis/collection/NCLCollectionStore/_Public/21/042/21042656.pdf)
- Hood, S.D., Nelson, C.S., Kamp, P.J.: Modification of fracture porosity by multiphase vein mineralization in an Oligocene nontropical carbonate reservoir, Taranaki Basin, New Zealand. *AAPG Bull.* **87**(10), 1575–1597 (2003)
- Huang, N., Jiang, Y., Liu, R., Li, B., Zhang, Z.: A predictive model of permeability for fractal-based rough rock fractures during shear. *Fractals* **25**(05), 1750051 (2017). <https://doi.org/10.1142/S0218348X17500517>
- Hyman, J.D., Karra, S., Makedonska, N., Gable, C.W., Painter, S.L., Viswanathan, H.S.: dfnWorks: a discrete fracture network framework for modeling subsurface flow and transport. *Comput. Geosci.* **84**, 10–19 (2015). <https://doi.org/10.1016/j.cageo.2015.08.001>
- Hyman, J.D., Aldrich, G., Viswanathan, H., Makedonska, N., Karra, S.: Fracture size and transmissivity correlations: Implications for transport simulations in sparse three-dimensional discrete fracture networks following a truncated power law distribution of fracture size. *Water Resour. Res.* **52**(8), 6472–6489 (2016). <https://doi.org/10.1002/2016WR018806>
- Jones, T.A., Detwiler, R.L.: Fracture sealing by mineral precipitation: the role of small-scale mineral heterogeneity. *Geophys. Res. Lett.* **43**(14), 069598 (2016). <https://doi.org/10.1002/2016GL069598>
- Karpyn, Z.T.: Induced rough fracture in Berea sandstone core. *Digit. Rocks Portal* (2016). <https://doi.org/10.17612/P7J012>
- Karpyn, Z.T., Grader, A.S., Halleck, P.M.: Visualization of fluid occupancy in a rough fracture using microtomography. *J. Colloid Interface Sci.* **307**(1), 181–187 (2007). <https://doi.org/10.1016/j.jcis.2006.10.082>
- Konzuk, J.S., Kueper, B.H.: Evaluation of cubic law based models describing single-phase flow through a rough-walled fracture: evaluation of cubic law based models. *Water Resour. Res.* **40**(2), W02402 (2004). <https://doi.org/10.1029/2003WR002356>
- Kresse, O., Weng, X., Gu, H., Wu, R.: Numerical modeling of hydraulic fractures interaction in complex naturally fractured formations. *Rock Mech. Rock Eng.* **46**(3), 555–568 (2013). <https://doi.org/10.1007/s00603-012-0359-2>
- Lander, R.H., Laubach, S.E.: Insights into rates of fracture growth and sealing from a model for quartz cementation in fractured sandstones. *Geol. Soc. Am. Bull.* **127**(3–4), 516–538 (2015)
- Landry, C.J., Karpyn, Z.T.: Single-phase lattice Boltzmann simulations of pore-scale flow in fractured permeable media. *Int. J. Oil Gas Coal Technol.* **5**(2–3), 182–206 (2012). <https://doi.org/10.1504/IJOGCT.2012.046320>
- Landry, C.J., Eichhubl, P., Prodanović, M., Wilkins, S.: Nanoscale grain boundary channels in fracture cement enhance flow in mudrocks: nanoscale grain boundary channels in fracture cement. *J. Geophys. Res. Solid Earth* **121**(5), 3366–3376 (2016). <https://doi.org/10.1002/2016JB012810>
- Lang, P.S., Paluszny, A., Zimmerman, R.W.: Permeability tensor of three-dimensional fractured porous rock and a comparison to trace map predictions. *J. Geophys. Res. Solid Earth* **119**(8), 6288–6307 (2014). <https://doi.org/10.1002/2014JB011027>
- Latt, J.: Palabos, parallel lattice Boltzmann solver (2009)
- Laubach, S.E., Diaz-Tushman, K.: Laurentian palaeostress trajectories and ephemeral fracture permeability, Cambrian Eriboll Formation sandstones west of the Moine Thrust Zone, NW Scotland. *J. Geol. Soc.* **166**(2), 349–362 (2009). <https://doi.org/10.1144/0016-76492008-061>
- Laubach, S., Reed, R., Olson, J., Lander, R., Bonnell, L.: Coevolution of crack-seal texture and fracture porosity in sedimentary rocks: cathodoluminescence observations of regional fractures. *J. Struct. Geol.* **26**(5), 967–982 (2004). <https://doi.org/10.1016/j.jsg.2003.08.019>

- Lei, Q., Latham, J.-P., Tsang, C.-F., Xiang, J., Lang, P.: A new approach to upscaling fracture network models while preserving geostatistical and geomechanical characteristics: a new fracture network upscaling method. *J. Geophys. Res. Solid Earth* **120**(7), 4784–4807 (2015). <https://doi.org/10.1002/2014JB011736>
- Lorenz, J. C.: Fracture Systems in the Piceance Basin: Overview and Comparison with Fractures in the San Juan and Green River Basins (2003). [http://archives.datapages.com/data/rmag/PiceanceBasin03/Lorenz\\_1.htm](http://archives.datapages.com/data/rmag/PiceanceBasin03/Lorenz_1.htm)
- Luczaj, J.A., Harrison, W.B., Smith Williams, N.: Fractured hydrothermal dolomite reservoirs in the Devonian Dundee Formation of the central Michigan Basin. *AAPG Bull.* **90**(11), 1787–1801 (2006). <https://doi.org/10.1306/06270605082>
- Luquot, L., Abdoulghafour, H., Gouze, P.: Hydro-dynamically controlled alteration of fractured Portland cements flowed by CO<sub>2</sub>-rich brine. *Int. J. Greenh. Gas Control* **16**, 167–179 (2013). <https://doi.org/10.1016/j.ijggc.2013.04.002>
- Matter, J.M., Kelemen, P.B.: Permanent storage of carbon dioxide in geological reservoirs by mineral carbonation. *Nat. Geosci.* **2**(12), 837–841 (2009). <https://doi.org/10.1038/ngeo683>
- Méheust, Y., Schmittbuhl, J.: Geometrical heterogeneities and permeability anisotropy of rough fractures. *J. Geophys. Res. Solid Earth* **106**(B2), 2089–2102 (2001). <https://doi.org/10.1029/2000JB900306>
- Noiriel, C., Renard, F., Doan, M.-L., Gratier, J.-P.: Intense fracturing and fracture sealing induced by mineral growth in porous rocks. *Chem. Geol.* **269**(3–4), 197–209 (2010). <https://doi.org/10.1016/j.chemgeo.2009.09.018>
- Ogilvie, S.R., Isakov, E., Glover, P.W.J.: Fluid flow through rough fractures in rocks. II: A new matching model for rough rock fractures. *Earth Planet. Sci. Lett.* **241**(3), 454–465 (2006). <https://doi.org/10.1016/j.epsl.2005.11.041>
- Olorode, O., Wang, B., Rashid, H.U.: Three-dimensional projection-based embedded discrete-fracture model for compositional simulation of fractured reservoirs. *SPE J.* **25**(04), 2143–2161 (2020). <https://doi.org/10.2118/201243-PA>
- Paluszny, A., Matthai, S.K.: Impact of fracture development on the effective permeability of porous rocks as determined by 2-D discrete fracture growth modeling. *J. Geophys. Res.* (2010). <https://doi.org/10.1029/2008JB006236>
- Pan, C., Luo, L.-S., Miller, C.T.: An evaluation of lattice Boltzmann schemes for porous medium flow simulation. *Comput. Fluids* **35**(8–9), 898–909 (2006). <https://doi.org/10.1016/j.compfluid.2005.03.008>
- Pandey, S.N., Chaudhuri, A., Rajaram, H., Kelkar, S.: Fracture transmissivity evolution due to silica dissolution/precipitation during geothermal heat extraction. *Geothermics* **57**, 111–126 (2015). <https://doi.org/10.1016/j.geothermics.2015.06.011>
- Phillips, A.J., Lauchnor, E., Eldring, J., Esposito, R., Mitchell, A.C., Gerlach, R., et al.: Potential CO<sub>2</sub> leakage reduction through biofilm-induced calcium carbonate precipitation. *Environ. Sci. Technol.* **47**(1), 142–149 (2013). <https://doi.org/10.1021/es301294q>
- Piggott, A.R., Elsworth, D.: Analytical models for flow through obstructed domains. *J. Geophys. Res. Solid Earth* **97**(B2), 2085–2093 (1992). <https://doi.org/10.1029/91JB02641>
- Taron, J., Elsworth, D.: Thermal–hydrologic–mechanical–chemical processes in the evolution of engineered geothermal reservoirs. *Int. J. Rock Mech. Min. Sci.* **46**(5), 855–864 (2009). <https://doi.org/10.1016/j.ijrmms.2009.01.007>
- Thomas, R.N., Paluszny, A., Zimmerman, R.W.: Permeability of three-dimensional numerically grown geomechanical discrete fracture networks with evolving geometry and mechanical apertures. *J. Geophys. Res. Solid Earth* **125**(4), e2019JB018899 (2020). <https://doi.org/10.1029/2019JB018899>
- Thompson, M.E., Brown, S.R.: The effect of anisotropic surface roughness on flow and transport in fractures. *J. Geophys. Res. Solid Earth* **96**(B13), 21923–21932 (1991). <https://doi.org/10.1029/91JB02252>
- Tokan-Lawal, A., Prodanović, M., Eichhubl, P.: Investigating flow properties of partially cemented fractures in Travis Peak Formation using image-based pore-scale modeling: flow in partially cemented fractures. *J. Geophys. Res. Solid Earth* **120**(8), 5453–5466 (2015a). <https://doi.org/10.1002/2015JB012045>
- Tokan-Lawal, A., Prodanović, M., Landry, C.J., Eichhubl, P.: Partially cemented tight sandstone fracture. *Digit. Rocks Portal* (2015b). <https://doi.org/10.17612/P7RP4Z>
- Tokan-Lawal, A., Prodanović, M., Landry, C.J., Eichhubl, P.: Influence of numerical cementation on multiphase displacement in rough fractures. *Transp. Porous Media* **25**, 1–19 (2016a)
- Tokan-Lawal, A., Prodanović, M., Eichhubl, P., Landry, C.J.: Niobrara formation fracture. *Digit. Rocks Portal* (2016b). <https://doi.org/10.17612/P7SG6Z>
- Tsang, Y.W.: The effect of tortuosity on fluid flow through a single fracture. *Water Resour. Res.* **20**(9), 1209–1215 (1984)

- Verma, A., Pruess, K.: Thermohydrological conditions and silica redistribution near high-level nuclear wastes emplaced in saturated geological formations. *J. Geophys. Res. Solid Earth* **93**(B2), 1159–1173 (1988). <https://doi.org/10.1029/JB093iB02p01159>
- Walsh, J.B.: Effect of pore pressure and confining pressure on fracture permeability. *Int. J. Rock Mech. Min. Sci. Geomech. Abstr.* **18**(5), 429–435 (1981). [https://doi.org/10.1016/0148-9062\(81\)90006-1](https://doi.org/10.1016/0148-9062(81)90006-1)
- Wennberg, O.P., Casini, G., Jonoud, S., Peacock, D.C.: The characteristics of open fractures in carbonate reservoirs and their impact on fluid flow: a discussion. *Pet. Geosci.* **22**(1), 91–104 (2016)
- Witherspoon, P.A., Wang, J.S.Y., Iwai, K., Gale, J.E.: Validity of cubic law for fluid flow in a deformable rock fracture. *Water Resour. Res.* **16**(6), 1016–1024 (1980)
- Yoon, H., Valocchi, A.J., Werth, C.J., Dewers, T.: Pore-scale simulation of mixing-induced calcium carbonate precipitation and dissolution in a microfluidic pore network. *Water Resour. Res.* **48**(2), W02524 (2012). <https://doi.org/10.1029/2011WR011192>
- Zimmerman, R.W., Bodvarsson, G.S.: Hydraulic conductivity of rock fractures. *Transp. Porous Media* **23**(1), 1–30 (1996)
- Zimmerman, R.W., Kumar, S., Bodvarsson, G.S.: Lubrication theory analysis of the permeability of rough-walled fractures. *Int. J. Rock Mech. Min. Sci. Geomech. Abstr.* **28**(4), 325–331 (1991). [https://doi.org/10.1016/0148-9062\(91\)90597-F](https://doi.org/10.1016/0148-9062(91)90597-F)
- Zimmerman, R.W., Chen, D.-W., Cook, N.G.W.: The effect of contact area on the permeability of fractures. *J. Hydrol.* **139**(1), 79–96 (1992). [https://doi.org/10.1016/0022-1694\(92\)90196-3](https://doi.org/10.1016/0022-1694(92)90196-3)

**Publisher's Note** Springer Nature remains neutral with regard to jurisdictional claims in published maps and institutional affiliations.

Springer Nature or its licensor (e.g. a society or other partner) holds exclusive rights to this article under a publishing agreement with the author(s) or other rightsholder(s); author self-archiving of the accepted manuscript version of this article is solely governed by the terms of such publishing agreement and applicable law.